JOURNAL OF GEOPHYSICAL RESEARCH, VOL. 97, NO. B3, PAGES 3235–3245, MARCH 10, 1992

An Analysis of Ridge Axis Gravity Roughness and Spreading Rate

CHRISTOPHER SMALL AND DAVID T. SANDWELL

Scripps Institution of Oceanography, La Jolla, California

Fast and slow spreading ridges have radically different morphologic and gravimetric characteristics. In this study, altimeter measurements from the Geosat Exact Repeat Mission (Geosat ERM) are used to investigate spreading rate dependence of the ridge axis gravity field. Gravity roughness provides an estimate of the amplitude of the gravity anomaly and is robust to small errors in the location of the ridge axis. We compute gravity roughness as a weighted root mean square (RMS) of the vertical deflection at 438 ridge crossings on the mid-ocean ridge system. Ridge axis gravity anomalies show a decrease in amplitude with increasing spreading rate up to an intermediate rate of ~60-80 mm/yr and almost no change at higher rates; overall the roughness decreases by a factor of 10 between the lowest and highest rates. In addition to the amplitude decrease, the range of roughness values observed at a given spreading rate shows a similar order of magnitude decrease with transition between 60 and 80 mm/yr. The transition of ridge axis gravity is most apparent at three relatively unexplored locations on the Southeast Indian Ridge and the Pacific-Antarctic Rise; on these intermediate rate ridges the transition occurs abruptly across transform faults.

INTRODUCTION

It is well known that mid-ocean ridge topography varies as a function of spreading rate [*Menard*, 1967]. Slow spreading ridges (15-30 mm/yr) are characterized by a deep (1-3 km) axial valley and rugged flanking topography while fast spreading ridges (100-160 mm/yr) are characterized by a small axial ridge and smoother flanking topography [*Macdonald*, 1986]. Free air gravity anomalies over fast and slow spreading ridges also reflect this difference in structure. Fast spreading ridges have small (<10 mGal) positive free air anomalies, while slow spreading ridges have larger (>30 mGal) negative anomalies flanked by positive anomalies [*Cochran*, 1979; *Small and Sandwell*, 1989]. Through an analysis of the gravity/topography transfer function over the Mid-Atlantic Ridge (MAR) and the East Pacific Rise (EPR), *Cochran* [1979] has shown that the gravity/topography ratio decreases with increasing spreading rate; this implies either a lithospheric elastic thickness which is dependent on spreading rate or a change in the mode of compensation. Overall, these results suggest that topography, gravity, and the gravity/topography ratio all vary with spreading rate, and perhaps their variations are all different. Here we make use of the uniform global coverage of satellite gravity data to investigate the amplitude of short-wavelength ridge axis gravity anomalies and to determine how the amplitude varies with spreading rate.

While the location of the entire mid-ocean ridge plate boundary is approximately known from compilations of underway bathymetry data, only a few areas have been mapped in detail. The majority of mid-ocean ridge surveys are made on the slow spreading central MAR and the fast spreading northern EPR because these sites are conveniently located and include the end-member examples. However, since our knowledge of mid-ocean ridges is based primarily on these surveys, almost nothing is known about the change in ridge axis morphology that occurs at the intermediate spreading rates. The major intermediate spreading rate ridges are located in remote southern ocean areas (i.e., Pacific Antarctic Rise and Southeast Indian Ridge) and thus have remained almost completely unsurveyed by ships.

At present, satellite altimeters provide the only source of data with sufficient accuracy and areal coverage to study the entire ridge system at a 10-km spatial resolution along widely spaced profiles (~80 km). High-accuracy (~1 μrad = 0.98 mGal) and high-resolution (~10 km half wavelength) vertical deflection profiles were obtained by averaging up to 44 repeat cycles from the Geosat Exact Repeat Mission (ERM) [*Sandwell and McAdoo*, 1990]. Using these new data, we performed a systematic analysis of the roughness of the gravity field over the global mid-ocean ridge system. In well-surveyed northern ocean areas, the Geosat ERM profiles confirm the shipboard measurements. In the poorly surveyed southern ocean areas, the Geosat ERM profiles provide new information on the gravity and state of isostasy of the ridge axis. This gravity roughness analysis supports our earlier finding that the ridge axis gravity signature does not change gradually with spreading rate but rather changes abruptly in specific locations which occur within a narrow range of intermediate rates [*Small and Sandwell*, 1989].

The main advantage of computing gravity roughness, instead of measuring the amplitude and polarity of the ridge axis anomaly, is that the roughness does not depend on a precise knowledge of the location of the ridge axis. As noted in our earlier study [*Small and Sandwell*, 1989], the polarity of the ridge axis anomaly can be ambiguous when the position of the ridge axis is uncertain by more than about 15 km. The calculation of gravity roughness removes this polarity ambiguity so that the results are not affected significantly by errors in ridge axis location. To further demonstrate the nature of the abrupt transition, we present a new gravity map of the southern Pacific-Antarctic Rise based on extremely dense altimeter coverage (~2-km track spacing). In this area there is no ambiguity in the location of the ridge axis; we observe a sharp transition from an axial high to an axial valley that occurs at a spreading rate of 64 mm/yr.

ESTIMATION OF GRAVITY ROUGHNESS

In this study, we consider roughness of the along-track vertical deflection as a measure of roughness of the gravity field. The vertical deflection is the along-track derivative of the geoid (i.e., sea

Paper number 91JB02465.
0148-0227/92/91JB-02465$05.00

surface slope) and is proportional to the horizontal component of the gravity anomaly vector. The procedure used to calculate stacked vertical deflection profiles from Geosat ERM data is discussed by *Sandwell and McAdoo* [1990]. Because the derivative operator acts as a high-pass filter, vertical deflection profiles tend to accentuate short-wavelength features while suppressing long-wavelength orbit errors and oceanographic effects.

A variety of methods can be used to estimate the roughness of a profile. The power spectrum provides a convenient summary of the distribution of energy as a function of wavelength. *Brown et al.* [1983] averaged the power over bands of wavenumbers to study geoid roughness using Seasat data. An advantage of this method is that it provides roughness estimates over a wide range of wavelengths. One limitation is that the profiles must be long enough to obtain reliable spectral estimates in the longest band, thus limiting the spatial resolution of the roughness map. *Gilbert et al.* [1989] use the envelope of band-pass-filtered Seasat data to estimate the geoid roughness for the South Atlantic. This method extracts the roughness in the shortest wave band which results in better spatial resolution.

Since we are primarily interested in the shortest-wavelength anomalies resolvable in the Geosat profiles, we have adopted a modified version of the *Gilbert et al.* [1989] method. Individual vertical deflection profiles are first band-pass filtered by convolution with Gaussian kernels. After high-pass and low-pass filters are applied, the roughness R_t at a given point t along the filtered profile is the weighted average of the squares of the surrounding values:

$$R_t = \left[\frac{1}{W} \sum_{i=-n}^{n} w_i \, \eta_{t+i}^2 \right]^{1/2}$$

where w_i are the individual weights, W is the sum of the weights, and η_{t+i} are the vertical deflections. The weights consist of $2n + 1$ samples of a Gaussian function with a range of $\pm 3\sigma$.

As would be expected, the roughness estimate is sensitive to the size of the window. Larger windows attenuate small-scale roughness variations, while narrower windows give a more localized roughness estimate with greater spatial resolution. Because the data are band-pass-filtered before roughness is computed, the mean is not removed from the estimate. Therefore, if the window is significantly narrower than the wavelength of a particular feature the roughness will appear to decrease near the inflection points and increase near the extrema. This becomes apparent if one considers a narrow window operating on a sinusoid, for which the roughness should remain constant. We have experimented with different window lengths and found that by setting the window length equal to the long-wavelength cutoff of the band-pass filter we can accurately detect the salient features in the data without introducing artifacts.

The selection of the long- and short-wavelength cutoffs for the band-pass filter is dictated by two factors: the characteristic wavelengths of the features being investigated and the resolution of the data. *Sandwell and McAdoo* [1990] have shown that a reasonable resolution limit for the 44-fold stacked Geosat ERM data is about 20 km. Thus 20 km is chosen as the short-wavelength cutoff. The selection of a long-wavelength cutoff is less straightforward and requires more careful consideration.

One way of establishing the proper long-wavelength cutoff is to analyze the power spectra of vertical deflection profiles. Profiles from two areas were selected for this analysis: a gravitationally smooth region in the eastern equatorial Pacific and a gravitationally rough region in the equatorial Atlantic (Figure 1). To obtain reliable

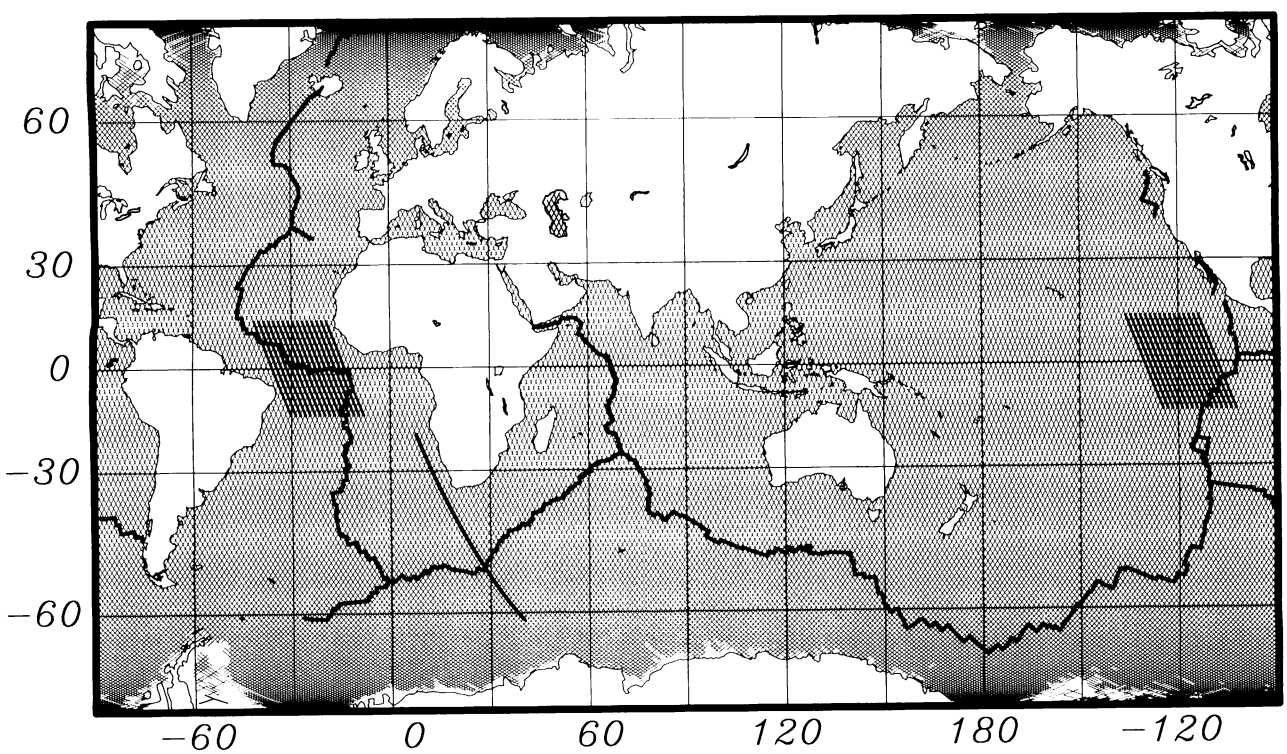

Fig. 1. Index map showing track coverage of the Geosat ERM and location of mid-ocean ridge plate boundary (thick line). Thick lines in the equatorial Atlantic and eastern Pacific show tracks used to estimate the power spectra of the vertical deflection profiles. Thick line south and west of Africa marks the profile shown in Figure 3.

spectral estimates, 16 profiles (1024 points long) were selected from each area. After windowing each profile, the power spectra were computed [*Welch*, 1967]. The composite spectra for each area are shown in Figure 2. At wavelengths longer than ~100 km, the spectra for both areas are relatively flat, and the Pacific data have about a factor of 10 less power than the Atlantic data. In each case there appears to be a natural corner frequency at ~100 km. For wavelengths less than 100 km the spectra of the rough and smooth areas decay at different rates. The spectral decay rate is related to the roughness of a surface [*Mandelbrot*, 1982]. For this reason, the difference in spectral slope for wavelengths between approximately 20 and 100 km is of particular interest.

Another method of establishing the long-wavelength cutoff is to compare the gravity profiles with topography profiles to determine the band where they have a high cross correlation. Cross spectral analyses of marine gravity and topography data have show high spectral coherence (and near zero phase) for wavelengths between 15 and 150 km [e.g., *Cochran*, 1979; *McNutt*, 1979]. Within this band both Airy and flexural compensation models also predict a high ratio of gravity to topography. For this reason we expect the vertical deflection roughness calculated in the 20-100 km band to be highly correlated with bathymetric roughness.

To demonstrate this high correlation between vertical deflection roughness and bathymetric roughness, we have compared profiles along coincident track lines. We chose example profiles from regions created at both slow and fast spreading ridges. Bathymetric roughness was computed from Sea Beam center-beam profiles using the methods described above. The first profile (slower spreading) was collected in the South Atlantic by the R/V *Conrad* in 1985 and runs from 8.4°S, 325.7°E to 28.1°S, 334.8°E along an ascending Geosat ground track. This 2400-km profile crosses several prominent fracture zones and a large seamount thus providing significant changes in both bathymetry and gravity roughness. The correlation coefficient between the vertical deflection roughness and bathymetry roughness is 0.95 for the entire profile and 0.88 for the ridge flanking portion of the profile excluding the seamount. A similar analysis was conducted for a Sea Beam profile collected in the eastern Pacific (faster spreading) by the R/V *Thomas Washington* in 1987. This 2900-km profile follows a descending Geosat ground track from 25°N, 235°E to 0°, 226°E and also provides several changes in topographic and gravimetric roughness. A comparison of this bathymetric roughness profile and the coincident satellite gravity roughness profile yielded a correlation coefficient of 0.97. Both examples demonstrate that in the 20-100 km wavelength band, variations in satellite gravity roughness accurately reflect variations in bathymetry roughness.

On the basis of these comparisons and the power spectral analyses shown in Figure 2, we adopted the 20-100 km wavelength range for our roughness analysis. The various processing steps are illustrated in Figure 3 for a profiles crossing the Southwest Indian Ridge (bottom profile, unfiltered; middle profile, band pass filtered; top profile, roughness estimate). Along-track vertical deflection roughness was calculated for all of the Geosat profiles shown in Figure 1. The roughness estimates were gridded to produce a global roughness map (Plate 1). (It should be noted that this map is used only to display the global data; individual roughness profiles are used for all of the quantitative analyses below.) The most striking feature of the global roughness map is the variation in roughness along the spreading ridges. The slow spreading ridges (e.g., Mid-Atlantic Ridge and Southwest Indian Ridge) show high roughness at the ridge axis (~15 μrad) and lower roughness (~6 μrad) on the flanks. In contrast, the fast spreading ridges (e.g., East Pacific Rise and northern Pacific-Antarctic Rise) show

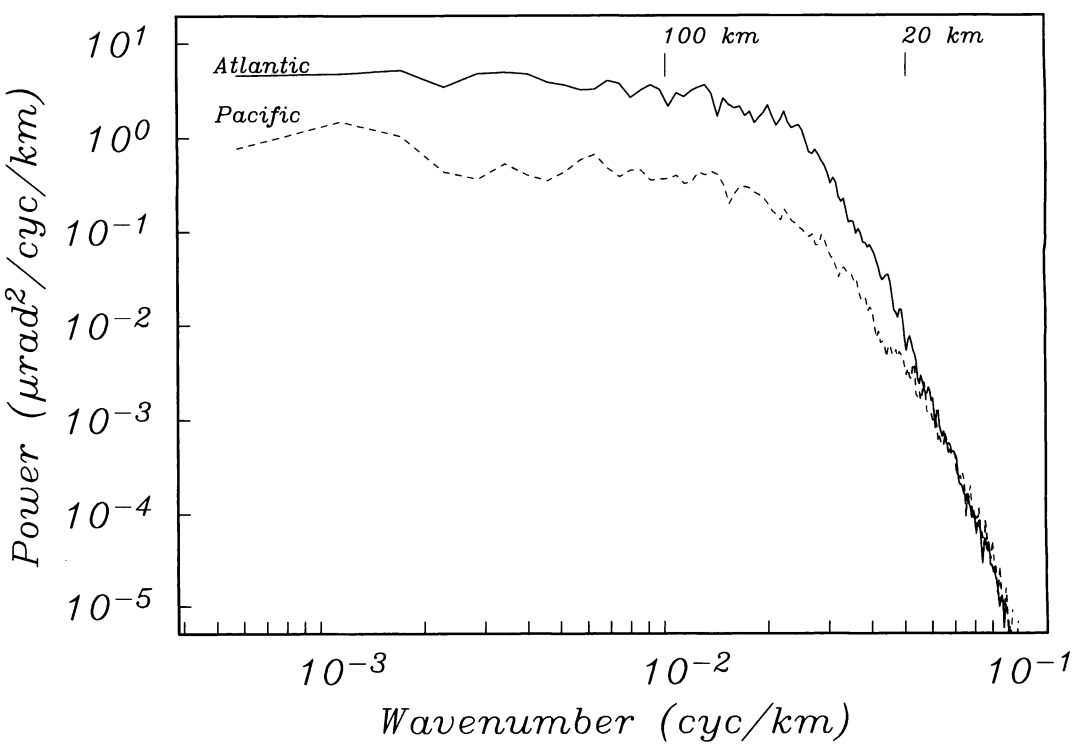

Fig. 2. Estimates of power spectra for vertical deflection profiles from two regions shown in Figure 1. Each spectrum is the composite of 16 profiles, 1024 points long. The Atlantic gravity field has more power than the Pacific at all wavelengths. Note the differences in the slopes of the power spectra between ~100 km and ~20 km.

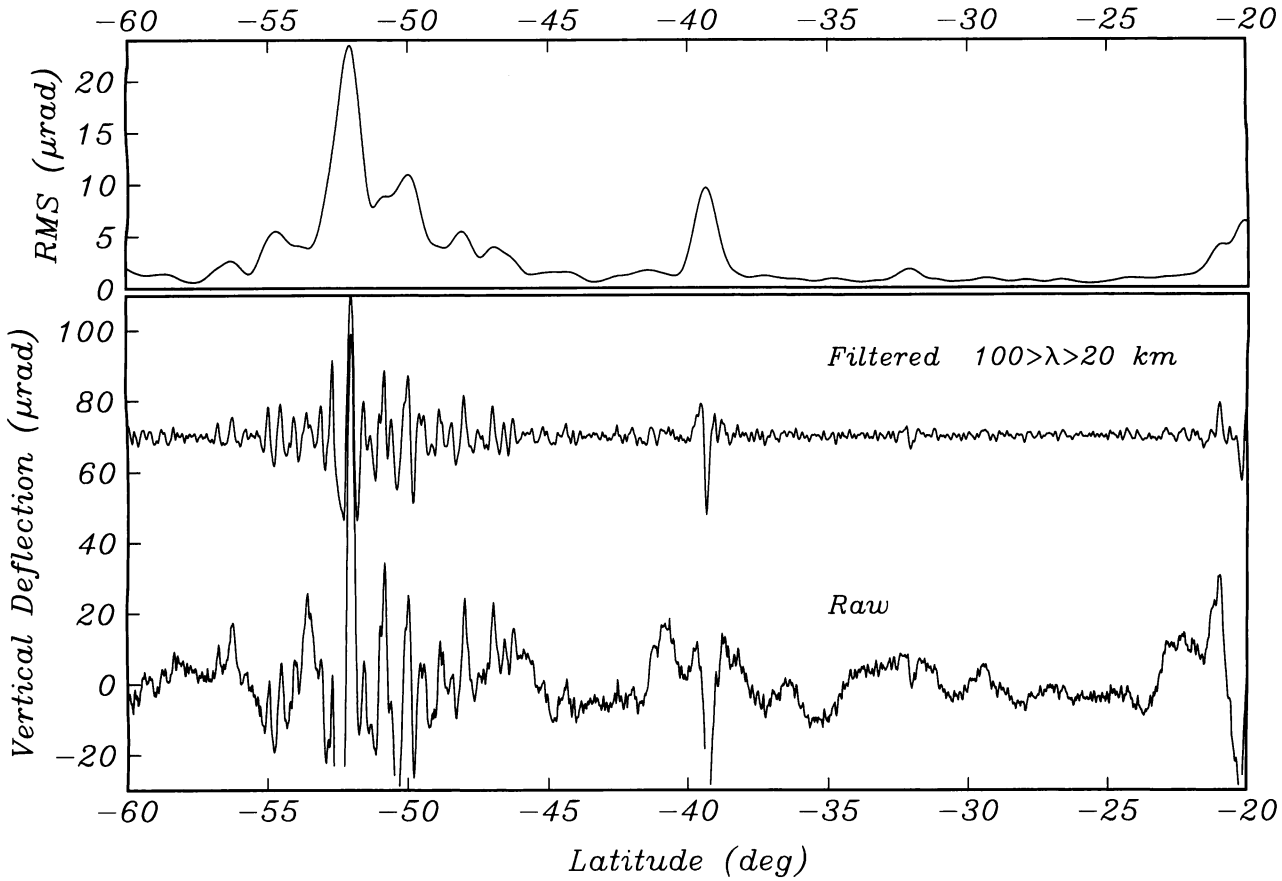

Fig. 3. Processing sequence: bottom, unfiltered vertical deflection profile; middle, profile after band-pass filtering ($20 < \lambda < 100$ km); top, along track roughness. The prominent feature near -52° is the anomaly due to the Southwest Indian Ridge. The smaller feature near -40° is anomaly of the Falkland Agulhas Fracture Zone. The anomaly near -20° results from the Walvis Ridge. The location of the profile is shown in Figure 1.

generally low roughness (< 2 μrad) on both the axis and the flanks (except near seamounts). In the remainder of this paper we provide a quantitative analysis of these first-order ridge axis roughness variations with special emphasis on the transition from high roughness to low roughness at intermediate spreading rates.

MID-OCEAN RIDGE PLATE BOUNDARY

The dynamics and structure of a mid-ocean ridge are certain to be influenced by the proximity of subduction zones (Chile Rise, Juan de Fuca, Gulf of California), the presence of large-scale propagating rifts (Easter microplate, Juan Fernandez microplate, Galapagos Rift) and the effects of continental rifting (Red Sea, Gulf of Aden). In this study we separate the continuous system into three major segments (Atlantic, Pacific, and Indian), smaller isolated ridges (Juan de Fuca, Cocos, Chile), and ridge segments which are known to be anomalous (Reykjanes Ridge, Australian-Antarctic Discordance Zone). In order not to complicate the analysis unnecessarily we have excluded continental rifts and propagating rifts.

We use a digitized plate boundary to define ridge and offset segments of the divergent plate boundaries. The plate boundary is derived primarily from published sources (Table 1), although some regions were digitized from GEBCO [*Canadian Hydrographic Service*, 1982] charts. Along the southern part of the Pacific Antarctic Rise, the plate boundary was determined from a high-resolution gravity map; this is discussed in the results section of this paper.

If one assumes that individual ridge segments and offsets (primarily transforms) can be approximated by line segments, then the plate boundary is described by the location of ridge transform intersections (RTIs). Once the RTIs are located, segments are identified as either ridges or transforms by comparing the azimuth of the segment to the azimuth of the plate motion vector at the midpoint of the segment. Plate motion azimuths and rates were computed using the NUVEL1 plate motion model [*DeMets et al.*, 1990]. We experimented with different criteria and found that the plate boundary could be represented accurately by categorizing any segment with an azimuth within ±45° of the plate motion vector as an offset and all others as ridge segments. Overlapping spreading centers were treated separately. The distribution of azimuths is strongly bimodal (as would be expected), and this scheme consistently picked alternating ridges and offsets correctly. An example of this procedure is shown in Figure 4. The vertical deflection profiles crossing the ridge segments are shown in Figure 5.

After calculating the along-track roughness profiles and identifying the ridge and transform segments, the roughness was extracted at the intersections of the satellite tracks and the plate boundary. Roughness values, spreading rates, intersection angles, and distances to the nearest RTI were computed for every intersection point. A total of 438 ridge crossings were detected.

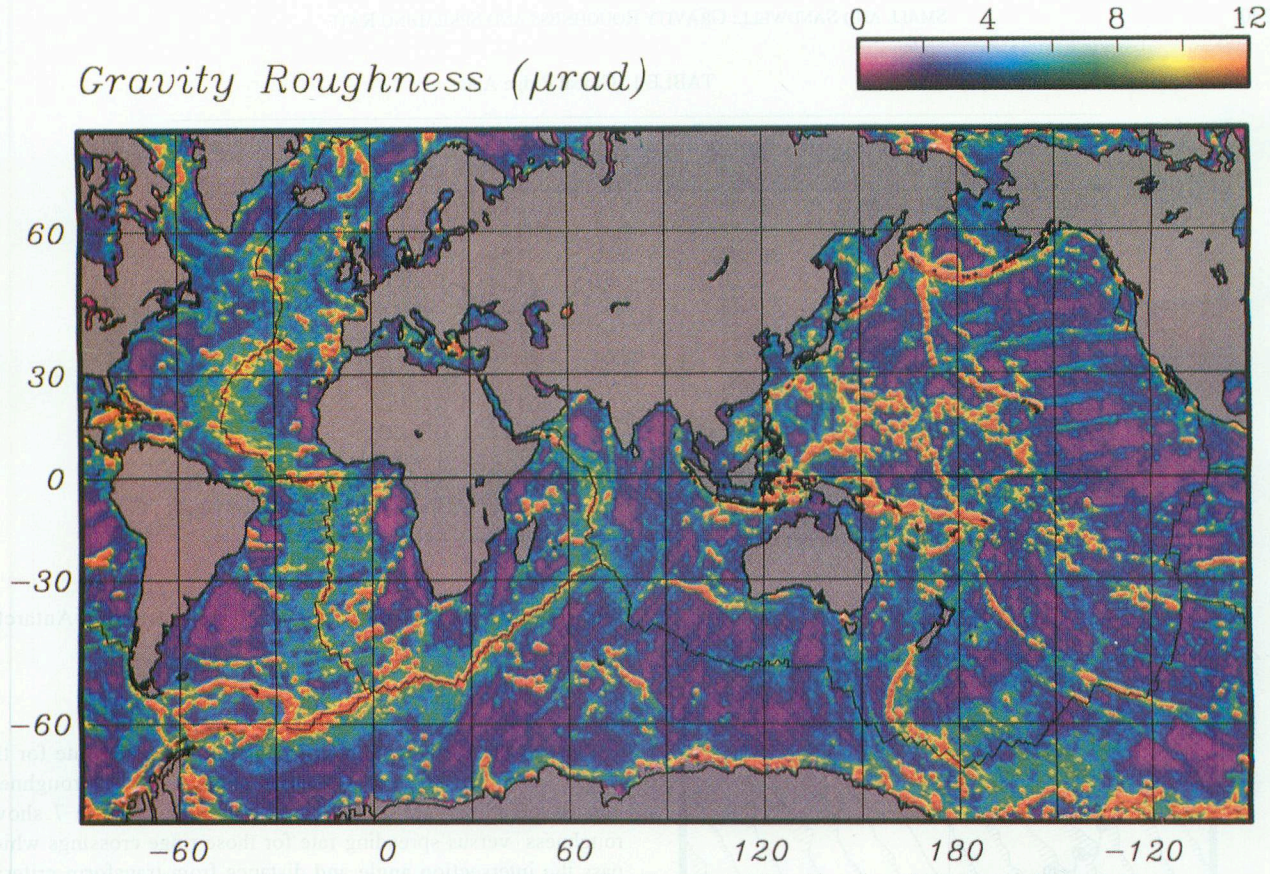

Plate 1. Global gravity roughness map gridded in 0.25° cells. Slower spreading ridges (e.g., Mid-Atlantic Ridge, Southwest Indian Ridge) have high flanking roughness and very high axial roughness. Roughness is low on both the axes and flanks of the fast spreading ridges (e.g., East Pacific Rise, northern Pacific-Antarctic Rise). Note the abrupt transition on the Southeast Indian Ridge and the bands of high roughness on the Pacific-Antarctic Rise flanks.

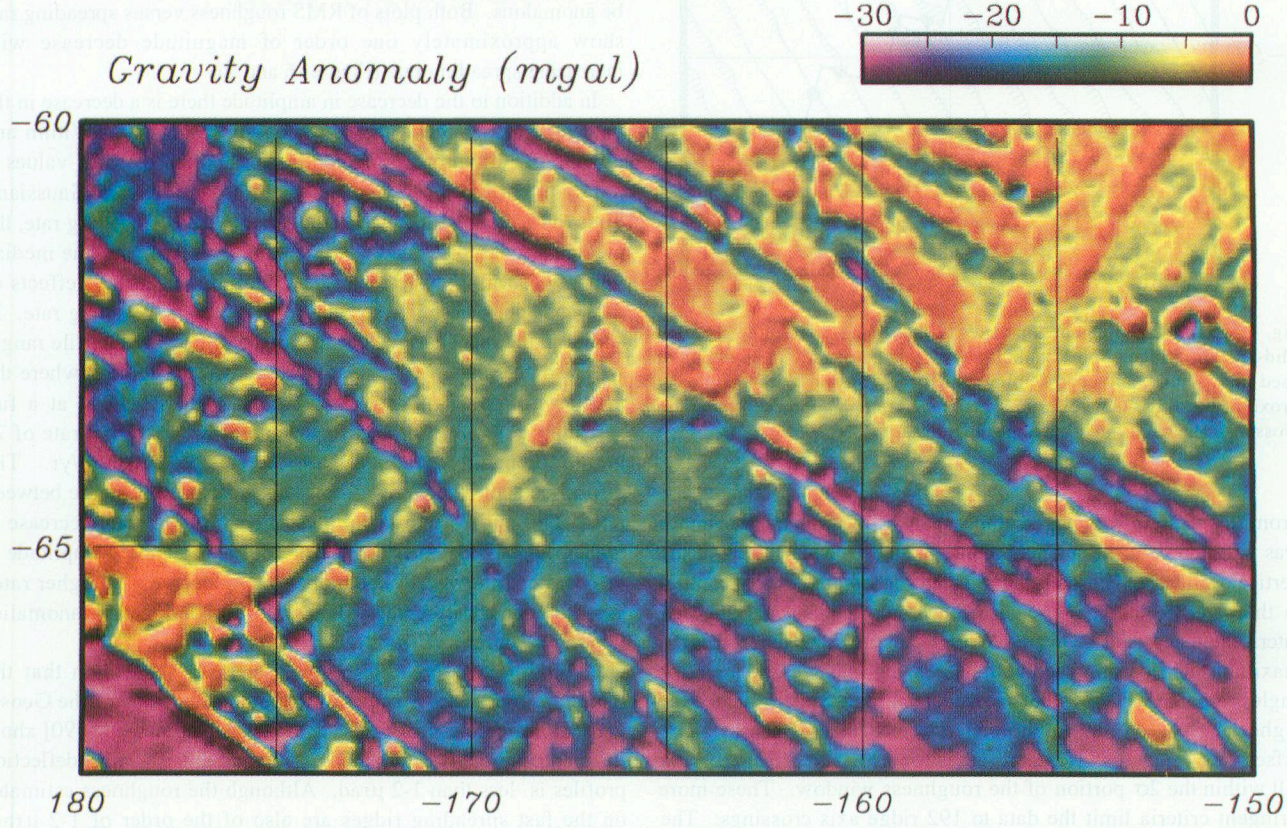

Plate 2. Free air gravity anomalies from closely spaced (~2 km) Geosat altimeter profiles on the Pacific-Antarctic Rise [*Sandwell*, 1991]. The linear anomaly oriented perpendicular to the direction of plate motion near (-65°, 185°) is interpreted as a ridge axis gravity low similar to that observed on slow spreading ridges. The linear high to the northeast (-64°, -162°) is interpreted as an axial high similar to that observed on fast spreading ridges. Note the abrupt decrease in fracture zone anomalies on younger crust near the ridge.

TABLE 1. Global Ridge Axis

Location	Range				References
	Latitude, deg	Longitude, deg	to Latitude, deg	Longitude, deg	
North Central Atlantic	50.06	331.00	15.26	314.88	*Klitgord and Schouten* [1986]
Equatorial Atlantic	15.26	314.88	5.65	327.03	*Cande et al.* [1988]
Equatorial Atlantic	5.65	327.03	0.30	343.50	*Roest* [1987]
Equatorial Atlantic	0.30	343.50	-6.02	348.74	GEBCO
South Atlantic	-6.02	348.74	-54.86	359.53	*Cande et al.* [1988]
Southwest Indian	-54.86	359.53	-25.64	69.96	*Royer et al.* [1988]
Central Indian	9.97	56.92	-25.64	69.96	*Royer et al.* [1988]
Southeast Indian	-25.64	69.96	-50.07	120.19	*Royer et al.*]1989]
Pacific-Antarctic	-34.60	249.43	-60.00	207.85	GEBCO
East Pacific Rise	-32.19	247.95	-26.45	247.14	GEBCO
East Pacific Rise	-23.09	245.44	0.44	257.73	*Lonsdale* [1989]
East Pacific Rise	0.44	257.73	2.45	257.39	*Atwater and Severinghaus* [1989]
East Pacific Rise	2.90	258.60	17.77	254.60	*Atwater and Severinghaus* [1989]

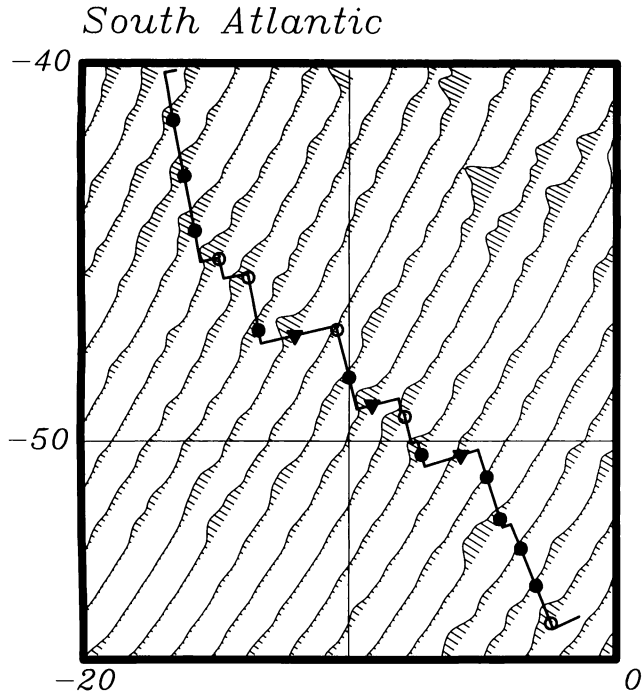

Fig. 4. Example of roughness profiles (20 μrad/deg) across the southern Mid-Atlantic Ridge. Solid symbols show location of roughness estimates used in the study, and open symbols show locations not used because of proximity to ridge-transform intersections. Triangles indicate transform crossings, and circles indicate ridge crossings.

From this data set we flagged all points for which the track azimuth was within 35° of the segment azimuth, since the amplitude of the vertical deflection is greatly diminished for features nearly parallel to the satellite track. When RMS was plotted as a function of intersection angle for all available ridge crossings, we found that the maximum RMS diminished with decreasing intersection angle for angles less than ~30°-35° but showed no azimuthal dependence for higher angles. In order to eliminate the influence of nearby ridge offsets, we flagged all ridge crossings for which an offset crossing fell within the 2σ portion of the roughness window. These more stringent criteria limit the data to 192 ridge axis crossings. The intersection angle criteria limited the number of measurements on the north-south trending EPR and MAR. The density of fracture zones on the MAR further limited the number of points available on this ridge as well as most points in the Australian-Antarctic Discordance Zone.

RESULTS

Plots of the RMS roughness versus full spreading rate for the ridges are shown in Figures 6 and 7. Figure 7 shows roughness versus spreading rate for all ridge crossings. Figure 7 shows roughness versus spreading rate for those ridge crossings which pass the intersection angle and distance from transform criteria. The subdivision of the ridge system discussed above is indicated with different symbols for the Atlantic, Pacific, and Indian ridge systems as well as the smaller ridges and those which are known to be anomalous. Both plots of RMS roughness versus spreading rate show approximately one order of magnitude decrease with increasing spreading rate (Figures 6 and 7).

In addition to the decrease in amplitude there is a decrease in the degree of dispersion with increasing spreading rate. Within any given range of spreading rates, the distribution of RMS values is not symmetric about the mean value (therefore non-Gaussian). Thus to further quantify RMS roughness versus spreading rate, the median was used instead of the mean. The length of the median window (15 mm/yr) was chosen to minimize spurious effects of data gaps and maximize resolution in terms of spreading rate. In addition, the dispersion about the median (i.e., interquartile range) was also calculated. The results are shown in Figure 7 where the median roughness decreases rapidly from 21 μrad at a full spreading rate of 15 mm/yr to a value of 3.0 μrad at a rate of 75 mm/yr then only gradually to 1.8 μrad at 150 mm/yr. The dispersion about the median shows a similar rapid decrease between rates of 15 and 75 mm/yr followed by a more gradual decrease at higher rates. The rapid decrease in ridge axis anomaly amplitude at lower rates followed by the more gradual decrease at higher rates agrees with our earlier study of peak-to-trough ridge axis anomalies [*Small and Sandwell*, 1989].

At the higher spreading rates, there is a suggestion that the minimum roughness may be limited by the accuracy of the Geosat vertical deflection profiles. *Sandwell and McAdoo* [1990] show that in most areas the estimated uncertainty in the vertical deflection profiles is less than 1-2 μrad. Although the roughness estimates on the fast spreading ridges are also of the order of 1-2 μrad, inspection of vertical deflection profiles shows that the ridge axis anomaly is usually distinct from the flanking anomalies [*Small and Sandwell*, 1989]. Furthermore, because the roughness estimate is

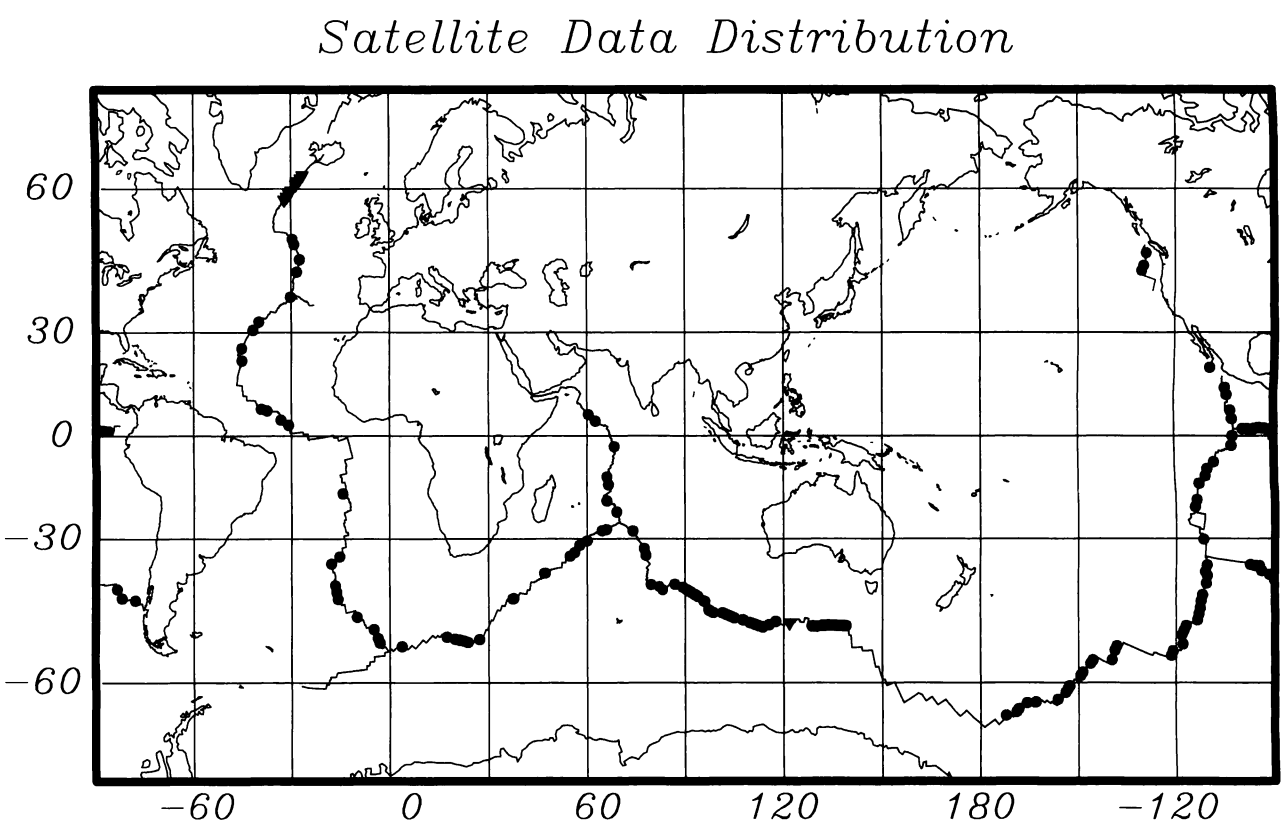

Fig. 5. Distribution of intersections (192) between Geosat profiles and the ridge axis. Only those crossings with intesection angles > 35° and more than 33 km from ridge-transform intersections are plotted. Crossings of anomalous ridges are indicated by triangles. The gap between 140° and ~180° longitude results from exclusion of the poorly mapped Pacific-Antarctic Rise.

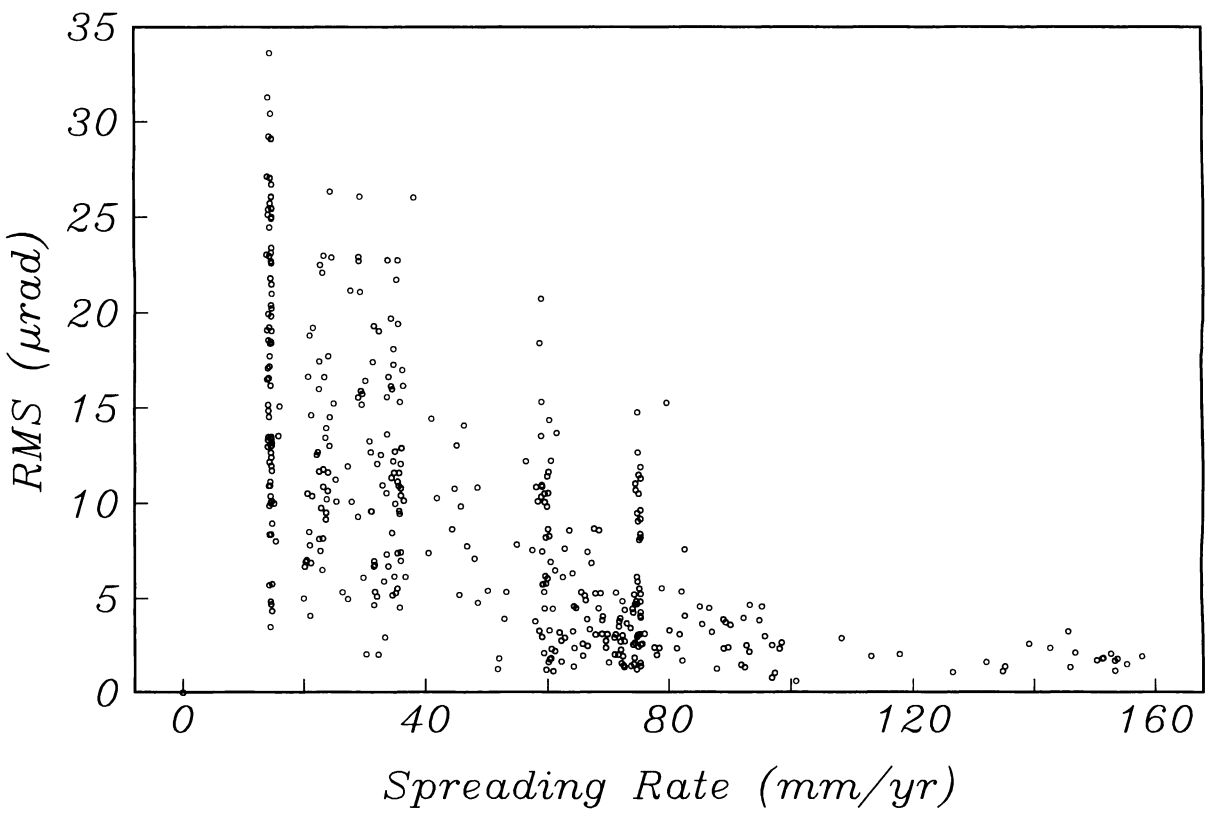

Fig. 6. Gravity roughness (RMS) versus full spreading rate for all ridge crossings. RMS roughness decreases by a factor of 10 between the lowest (16 mm/yr) and highest (155 mm/yr) spreading rates. Beyond 80 mm/yr, roughness is uniformly low.

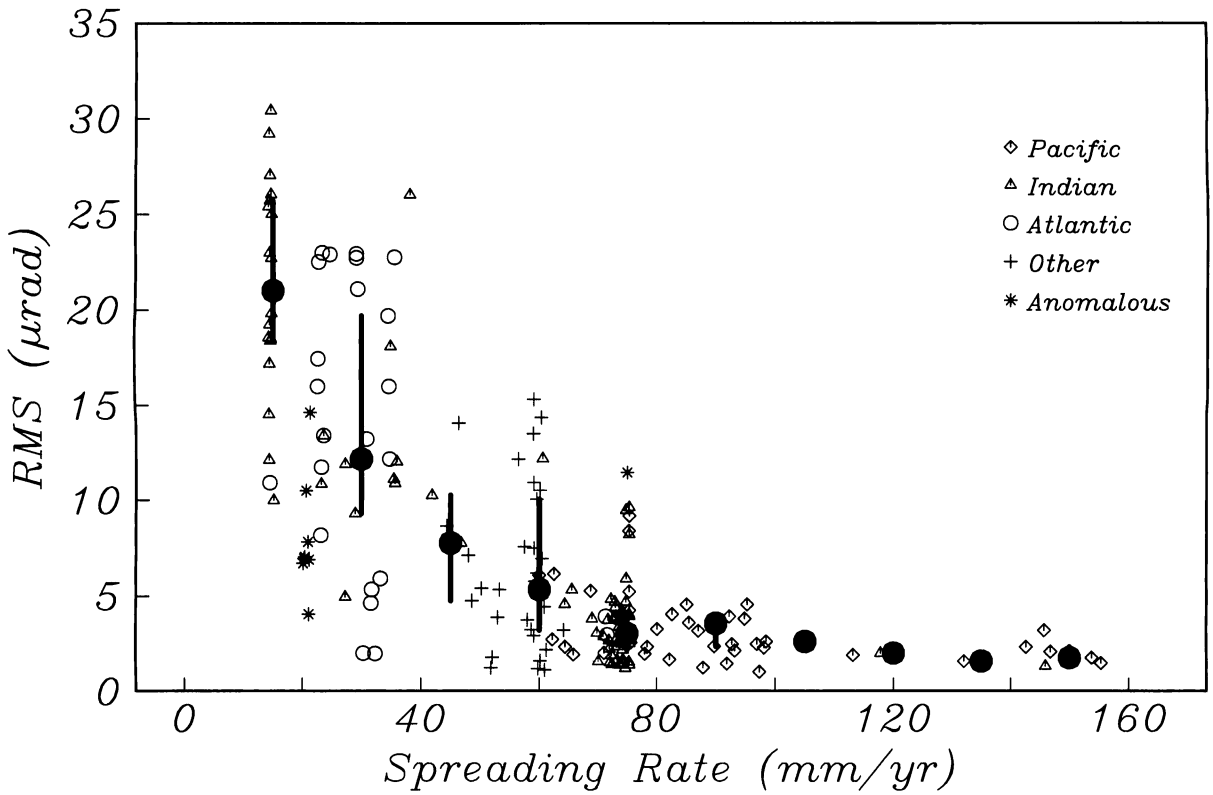

Fig. 7. Gravity roughness versus full spreading rate for ridge crossings > 33 km from a RTI and > 35° intersection angle. Open symbols indicate individual crossings from different ridges. Solid circles indicate median RMS roughness, and vertical bars indicate the interquartile range. A 15 mm/yr window was used. Median RMS roughness decreases from 21 μrad at 15 mm/yr to 5.3 μrad at 60 mm/yr. At higher rates (75-150 mm/yr), the decrease is much more gradual (3.0-1.8 μrad).

an average within the window, roughness values will always underestimate peak values for narrow anomalies. Thus we believe that the 1-2 μrad value at fast spreading ridges reflects the true roughness rather than the limitations of the data

To further investigate the spreading rate transition in ridge axis gravity roughness shown in Figures 6 and 7, we have studied the intermediate rate ridges in more detail. There are five regions of the global mid-ocean ridge system where spreading occurs at intermediate rates. In order to minimize the number of factors influencing the ridge axis dynamics we emphasize those within the continuous ridge system which might be considered "typical". The Chile Rise and the Juan de Fuca Ridge are spreading at intermediate rates, but they are both directly adjacent to active subduction zones and neither is part of the primary ridge system. In addition, the East Pacific Rise spreads at an intermediate rate in the vicinity of the mouth of the Gulf of California, but this area is also adjacent to the edge of an active subduction zone and the recent continental rifting of the Gulf of California. The best examples of intermediate spreading rate ridges are the Southeast Indian Ridge and the Pacific-Antarctic Rise. Unfortunately, both of these ridges lie in relatively unexplored regions of the southern oceans where underway shipboard data are sparse. Since satellite altimetry provides the most complete, consistent coverage available for such remote regions, we have conducted a more detailed study of these ridges with the available altimeter data.

The Southeast Indian Ridge forms part of a continuous segment stretching from the Gulf of Aden through the central Indian Ocean to the Rodriguez Triple Junction and through the southeast Indian Ocean to the Australian-Antarctic Discordance Zone. Along this ridge, spreading rates increase from ~25 mm/yr near the Gulf of Aden to ~45 mm/yr at the Rodriguez Triple Junction to ~70 mm/yr at Amsterdam and St. Paul islands to ~76 mm/yr near the Discordance Zone. Figure 8 shows descending vertical deflection profiles along this section of ridge. Both axial and flanking anomaly amplitudes decrease southeastward along the ridge axis between the Rodriguez Triple Junction and Amsterdam and St. Paul islands. Eastward from Amsterdam and St. Paul, anomaly amplitudes remain low but then increase abruptly near 100°E.

This effect is seen more clearly in Figure 9, where ridge axis gravity roughness is plotted versus longitude along the ridge. There is a rapid, order of magnitude, decrease in roughness between spreading rates of 27 and 69 mm/yr followed by low roughness values at higher rates (70-76 mm/yr) eastward to 100°E, where the roughness again increases. Available bathymetric data also show a transition from an axial valley to an axial high in the vicinity of Amsterdam and St. Paul islands [*Royer*, 1985; *Royer and Schlich*, 1988; R.L. Fisher, personal communication, 1991]. *Small and Sandwell* [1989] also found a transition from an axial low to an axial high in gravity anomlies in this region. It is interesting to note that the roughness increases again near 100°E, although the spreading rate does not change significantly (76 mm/yr). Although it is possible that our ridge axis is mislocated between 110° and 115°, this would not explain the variations in both axial and flanking roughness on adjacent profiles between 100° and 110°E. These observations are consistent with results of a recent study by Cochran [1991] which showed an abrupt change in axial morphology, flanking roughness and magnetic anomaly amplitude near 100°E.

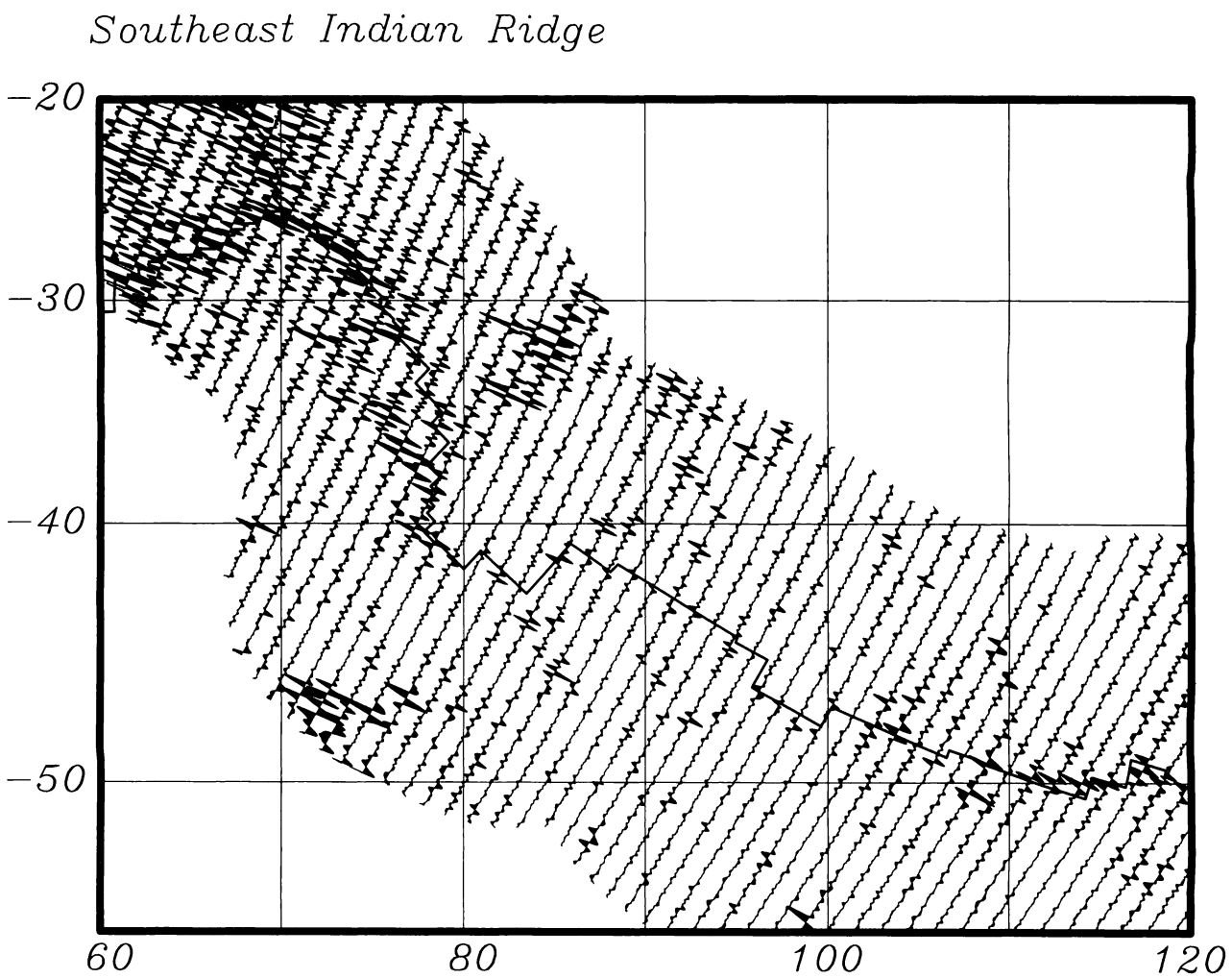

Fig. 8. Descending Geosat vertical deflection profiles along the Southeast Indian Ridge. Vertical deflections within 500 km of the ridge are plotted along satellite tracks at a scale of 20 μrad/deg with positive anomalies filled. The plate boundary is indicated by the thick line. Note the abrupt decrease in amplitude of both axial and flanking anomalies to the east of ~78°E.

The Pacific-Antarctic Rise is a second location along the primary ridge system where spreading occurs at intermediate rates. Recent declassification of data from the Geosat Geodetic Mission (GM) south of 60°S allow a much more detailed view of the gravity field along the Pacific-Antarctic Rise. The dense track spacing of the GM data allows a complete two-dimensional gravity field to be derived from vertical deflection profiles [*Sandwell*, 1991]. Gravity anomalies for this area are shown in Plate 2. While axial gravity roughness in this area does not change drastically, it is apparent from Plate 2 that the character of the axial gravity anomaly does. The westernmost ridge segment (-175° to -170° longitude, 60 mm/yr) clearly shows an axial valley anomaly (i.e., a linear gravity low flanked by highs oriented perpendicular to the fracture zone anomalies). The region to the northeast of this segment (-170° to -164° longitude, 64 mm/yr) shows almost no linear axial anomaly. Finally, the region to the east of -164° (71 mm/yr) clearly shows axial ridge anomalies (i.e., axial highs perpendicular to the fracture zone anomalies). Thus there is a clear transition from axial valley to axial high that occurs over a narrow range of spreading rates (60-71 mm/yr) Although underway data in this area are scarce, available bathymetric profiles confirm this transition from an axial valley to an axial ridge.

DISCUSSION

It is apparent from Figures 6 and 7 that there is a pronounced change in the amplitude and variability of *ridge axis* gravity anomalies that occurs between spreading rates of ~60 and 80 mm/yr. The distribution of points in the 60-100 mm/yr range of spreading rates is sufficient to demonstrate that this change is real and not a result of poor sampling at intermediate rates. While it may be argued that gravity roughness varies continuously with spreading rate, as has been proposed by *Malinverno* [1991] for ridge flank bathymetry roughness, we feel that the abrupt decrease in amplitude variability and the transition in axial anomaly polarity [*Small and Sandwell*, 1989] indicate an abrupt transition. This interpretation seems to be supported by the spatially abrupt transitions in the three regions discussed above.

This decrease in gravity roughness with increasing spreading rate is also apparent in the global gravity roughness map in Plate 1; slow spreading ridges have large amplitude axial anomalies, while fast spreading ridges have small-amplitude anomalies and the transition between the two is quite abrupt. However, in addition to the change in the ridge axis anomalies, the global roughness map shows that the gravity roughness on the ridge flanks also decreases with

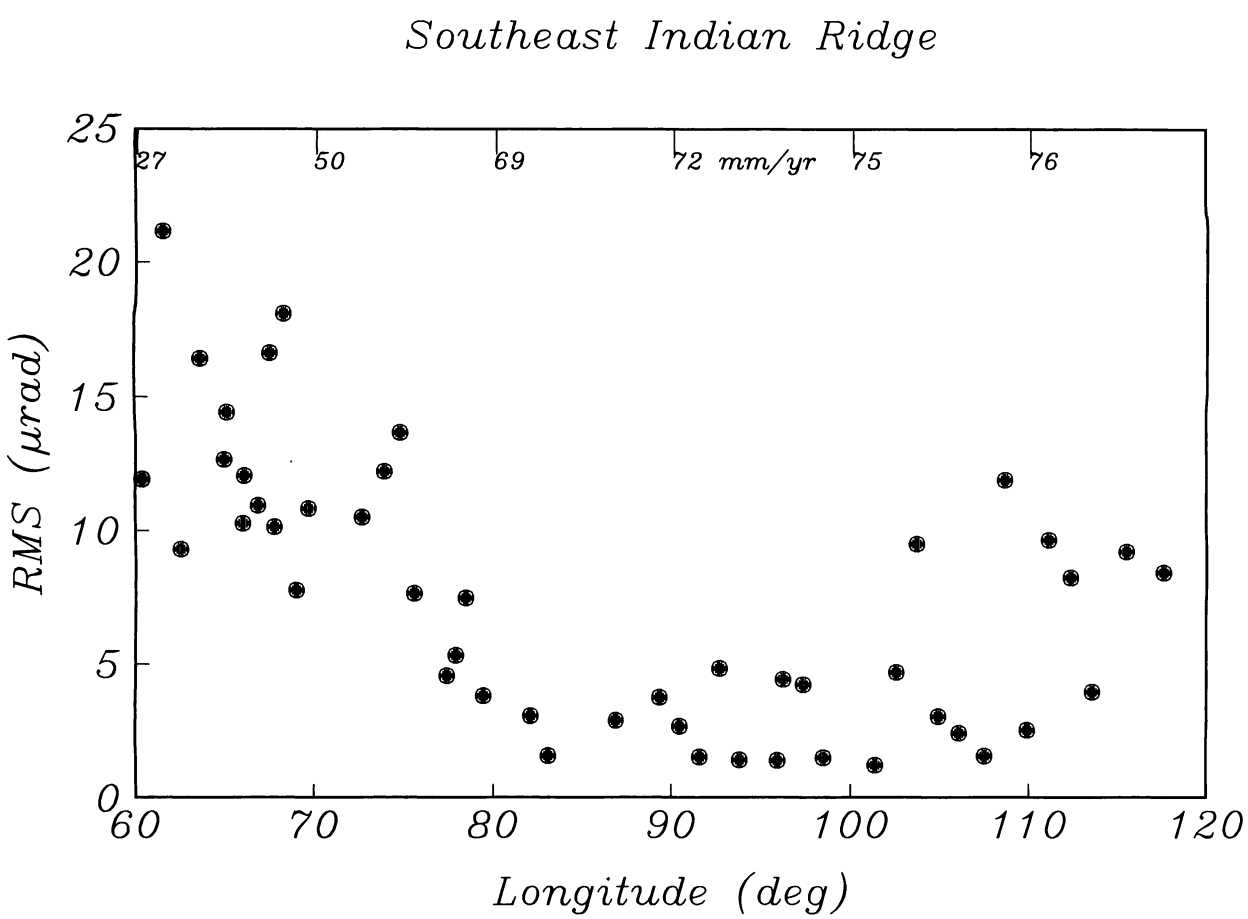

Fig. 9. Gravity roughness (RMS) plotted as a function of longitude for ridge axis anomalies shown in Figure 8. On the western end of the ridge these data show a pattern similar to that of the global data set with a rapid decrease in roughness between rates of 27 and 69 mm/yr followed by uniform roughness at rates greater than ~70 mm/yr. Farther to the east the roughness again increases abruptly near 100°E and varies between 2 and 13 μrad eastward to the Australian-Antarctic Discordance Zone.

increasing spreading rate. This is consistent with the observation that slow spreading ridges have rougher flanking topography than fast spreading ridges [*Menard*, 1967; *Malinverno*, 1991; *Hayes and Kane*, 1991]. The relationship of gravity roughness to topographic roughness on the ridge flanks is more complicated, however, because of sedimentation, changes in water depth and the presence of fracture zones. The relative scarcity of satellite tracks which follow plate motion flowlines would seem to preclude a simple comparison of our ridge flank roughness data with the results obtained by *Malinverno* [1991] for ridge flank bathymetric roughness. While the transition in flanking roughness is probably related to the abrupt transition in axial roughness, an analysis of the flanking roughness is considerably more involved and will be discussed in a separate study.

Although the transition shown in Figure 6 spans the range of spreading rates from ~60 to 80 mm/yr, examination of the regions discussed above indicates that the transition is spatially abrupt within this range of spreading rates. The limited bathymetric data available indicate that these transition zones are accompanied by changes in axial morphology [*Royer*, 1985; *Cochran*, 1991]. This is consistent with the findings of our previous study [*Small and Sandwell*, 1989] in which we found changes in the polarity of axial anomalies in this range of spreading rates.

If the change from variable, high-amplitude gravity anomalies to uniform, low-amplitude axial gravity anomalies reflects a change in the process of crustal accretion, then it is clearly dependent on other factors in addition to spreading rate. Mantle temperature and melt distribution (e.g., crustal thickness) would be expected to exert a strong influence on the axial morphology and compensation mechanism [*Chen and Morgan*, 1990]. This is consistent with our observations. For example, the transition from an axial valley to an axial ridge on the Reykjanes Ridge occurs at a spreading rate of ~20 mm/yr, which is not within the 60-80 mm/yr transition range of the majority of the ridges. Elevated mantle temperatures and excess melt are expected on the Reykjanes Ridge as a result of the proximity of the Iceland hot spot. Likewise, lower temperatures and diminished melting are inferred for the Australian-Antarctic Discordance Zone (~74 mm/yr), where a deep axial valley and large amplitude axial gravity anomalies are present [*Marks et al.*, 1990; *Klein and Langmuir*, 1987; *Christie et al.*, 1988].

The distribution of offsets in the ridge may also affect the axial structure. Along the Reykjanes Ridge, where the axial morphology is more typical of a fast spreading ridge, there is an absence of large transform offsets. Along the Southeast Indian Ridge, the average distance between significant transform offsets increases abruptly near Amsterdam and St. Paul islands where the anomaly amplitude decreases. The axial anomaly amplitude begins to increase toward the discordance zone where the distance between transform offsets begins to decrease. Although the abundance of fracture zones eliminated all but one of our roughness measurements in the

discordance zone, inspection of the vertical deflection profiles indicates a large amplitude anomalies consistent with the deep axial valley which is known to be present. *Cochran* [1991] also finds that transitions in axial morphology and flanking roughness occur across transform offsets in the vicinity of 100°E on the Southeast Indian Ridge. On the Pacific-Antarctic Rise, shown in Plate 2, the gravity anomalies on the ridge flanks seem to show several abandoned fracture zones, possibly indicating a recent change in the plate boundary geometry. If this is the case, then this ridge segment may currently be in the process of changing modes of accretion. If crustal accretion at the ridge axis is controlled by mantle temperature and melt distribution, then transform offsets would effectively segment the ridge thereby controlling the axial structure.

The data presented here seem to indicate that ridge axis structure changes abruptly in certain locations which occur at intermediate spreading rates of ~60-80 mm/yr. Although it is unlikely that spreading rate is the only factor affecting ridge structure, it is certainly an important and possibly dominant control. Without detailed surveys of these transition zones we cannot determine the relative importance of these factors, but it should be apparent that intermediate spreading rate ridges are critical to our understanding of the system as a whole.

Acknowledgments. We thank Karen Marks for suggesting a global gravity roughness study. John Chen, Peter Lonsdale, Dan McKenzie, and Walter Smith also contributed useful comments and suggestions. In addition, we thank Jim Cochran and Marcia McNutt for careful reviews. Chris Small was supported by the NSF Marine Geology and Geophysics Program (OCE89-22751). David Sandwell was supported by Scripps Inststution of Oceanography and NASA Solid Earth Sciences Program (NAG 1266).

REFERENCES

Atwater, T., and J. Severinghaus, *The Geology of North America*, vol. N, *Tectonic Maps of the Northeast Pacific*, Geological Society of America, Boulder, Colo., 1989.

Brown, R.D., W.D. Kohn, D.C. McAdoo, and W.E. Himwich, Roughness of the marine geoid from Seasat altimetry, *J. Geophys. Res.*, *88*, 1531-1540, 1983.

Canadian Hydrographic Service, General bathymetric map of the oceans (GEBCO), scale 1:10,000,000, Ottawa, Ont., 1982.

Cande, S., J. L. LaBrecque, and W.B. Haxby, Plate kinematics of the South Atlantic: Chron 34 to present, *J. Geophys. Res.*, *93*, 13,479-13,492, 1988.

Chen, Y., and W.J. Morgan, A nonlinear rheology model for mid-ocean ridge topography, *J. Geophys. Res.*, *95*, 17,583-17,604, 1990.

Christie, D.M., D. Pyle, J.-C. Sempere, J.P. Morgan, and A Shor, Petrologic and tectonic observations in and adjacent to the Australian-Antarctic Discordance, *Eos Trans. AGU, 69*, 1426, 1988.

Cochran, J.R., An analysis of isostasy in the world's oceans, 2, Mid-ocean ridge crests, *J. Geophys. Res.*, *84*, 4713-4729, 1979.

Cochran, J.R., Systematic variation of axial morphology along the Southeast Indian Ridge, *Eos Trans. AGU*, *72*, 260, 1991.

DeMets, C.,R.G. Gordon, D.F. Argus, and S. Stein, Current plate motions, *Geophys. J. Int.*, *101*, 425-478, 1990.

Gilbert, D., V. Courtillot, and J.L. Olivet, Seasat altimetry and the South Atlantic geoid 2, Short-wavelength undulations, *J. Geophys. Res.*, *94*, 5545-5559, 1989.

Hayes, D.E., and K.A. Kane, The dependence of seafloor roughness on spreading rate, *Geophys. Res. Lett.*, *18*, 1425-1428, 1991.

Klein, E.M., and C.H. Langmuir, Global correlations of oceanic ridge basalt chemistry with axial depth and crustal thickness, *J. Geophys. Res.*, *92*, 8089-8115, 1987.

Klitgord, K.D., and H. Schouten, Plate kinematics of the central Atlantic, in *The Geology of North America*, vol. M, *The Western North Atlantic Region*, edited by P.R. Vogt and B.E. Tucholke, pp. 351-378, Geological Society of America, Boulder, Colo., 1986

Lonsdale, P., Segmentation of the Pacific-Nazca Spreading Center, 1°N-20°S, *J. Geophys. Res.*, *94*, 12,197-12,225, 1989.

Macdonald, K.C., The crest of the Mid-Atlantic Ridge: Models for crustal generation and tectonics, in *The Geology of North America*, vol. M, *The Western North Atlantic Region*, edited by P.R. Vogt and B.E. Tucholke, pp. 51-68, Geological Society of America, Boulder, Colo., 1986.

Malinverno, A., Inverse square-root dependence of mid-ocean ridge flank roughness on spreading rate, *Nature*, *352*, 58-60, 1991.

Mandelbrot, B., *The Fractal Geometry of Nature*, 460 pp. W.H. Freeman, San Francisco, New York, 1982.

Marks, K.M., and R.V. Sailor, Comparison of GEOS 3 and Seasat altimeter resolution capabilities, *Geophys. Res. Lett.*, *7*, 193-196, 1980.

Marks, K.M., P.R. Vogt , and S.A. Hall, Residual depth anomalies and the origin of the Australian-Antarctic discordance zone., *J. Geophys. Res.*, *95*, 17,325-17,337, 1990.

McNutt, M., Compensation of ocean topography: An application of the response funciton technique to the *Surveyor* area, *J. Geophys. Res.*, *84*, 7589-7598, 1979.

Menard, H.W., Seafloor spreading, topography and the second layer, *Science*, *157*, 923-924, 1967.

Roest, W.R., Seafloor spreading patterns of the North Atantic between 10° and 40°N, *Geol. Ultraiectina*, *48*, 121 pp., 1987.

Royer, J.-Y., Evolution cinematique detaillee de la dorsale est-indienne entre le point triple de Rodriguez et les iles Amsterdam et Saint Paul pendant les 20 derniers millions d'annees, these de doctorat, 213 pp., Univ. Louis Pasteur, Strasbourg, France, 1985.

Royer, J.-Y., P. Patriat, H.W. Bergh, and C.R. Scotese, Evolution of the Southwest Indian Ridge from the Late Cretaceous (anomaly 34) to the middle Eocene (anomaly 20), *Tectonophysics*, *155*, 235-260, 1988.

Royer, J.-Y., and R. Schlich, Southeast Indian Ridge between the Rodriguez Triple Junction and the Amsterdam and Saint-Paul islands: Detailed kinematics for the past 20 m.y., *J. Geophys. Res.*, *93*, 13,524-13,550, 1988.

Royer, J.-Y., J.G. Sclater, and D.T. Sandwell, A preliminary tectonic fabric chart of the Indian Ocean, *Proc. Indian Acad. Sci.*, *98*, 7-24, 1989.

Sandwell, D.T., and D.C. McAdoo, High-accuracy, high-resolution gravity profiles from 2 years of the Geosat Exact Repeat Mission, *J. Geophys. Res.*, *95*, 3049-3060, 1990.

Sandwell, D.T., Antarctic marine gravity field from high density satellite altimetry, *Geophys. J. Int.*, in press, 1991.

Small, C., and D.T. Sandwell, An abrupt change in ridge axis gravity with spreading rate, *J. Geophys. Res.*, *94*, 17,383-17,392, 1989.

Welch, P.D., The use of the fast Fourier transform for estimation of power spectra: A method based on time averaging over short modified periodograms, *IEEE Trans. Audio Electroacoust.*, *AU15*, 70-73, 1967.

D.T. Sandwell and C. Small, Scripps Institution of Oceanography, Geological Research Division, 9500 Gilman Drive, La Jolla, CA 92093-0220.

(Received March 23, 1991;
Revised September 23, 1991;
accepted September 25, 1991.)